Supplementary information for:

Nanofiller-conjugated percolating conductive network modified polymerization reaction characteristics of aromatic thermosetting copolyester resin

Mete Bakir[a], Jacob L. Meyer[a,d], Andre Sutrisno[c], James Economy[b,d], Iwona Jasiuk[a,*]

a) Department of Mechanical Science and Engineering, University of Illinois at Urbana-Champaign, Urbana, IL 61801, USA.

b) Department of Materials Science and Engineering, University of Illinois at Urbana-Champaign, Urbana, IL 61801, USA.

c) NMR/EPR Laboratory, School of Chemical Sciences, University of Illinois at Urbana-Champaign, Urbana, IL 61801, USA

d) ATSP Innovations, Champaign, IL 61820, USA.

* Correspondence to Iwona Jasiuk. Email: ijasiuk@illinois.edu

Telephone Number: +1-217-333-92-59

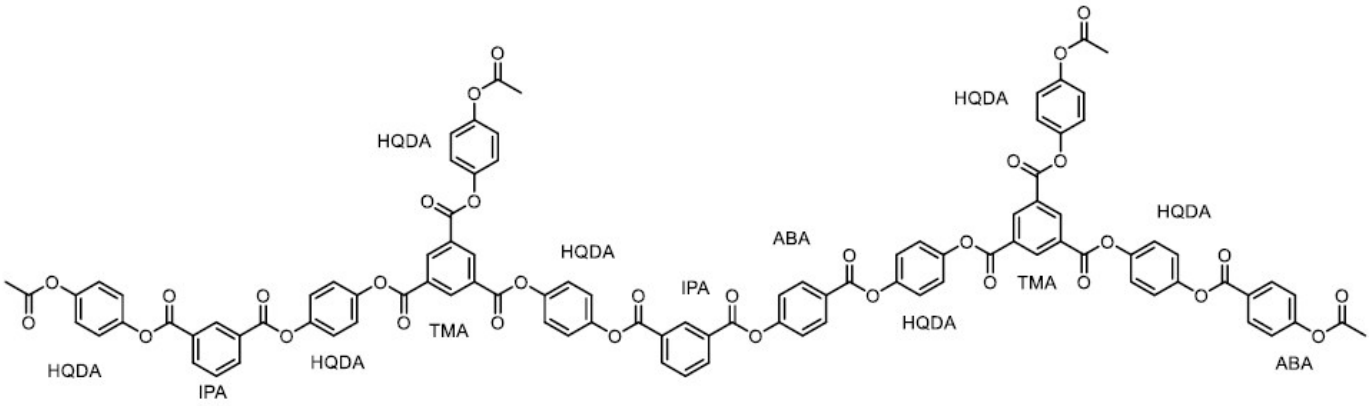

Figure S1. Chemical structure of aromatic acetoxy end-group oligomer

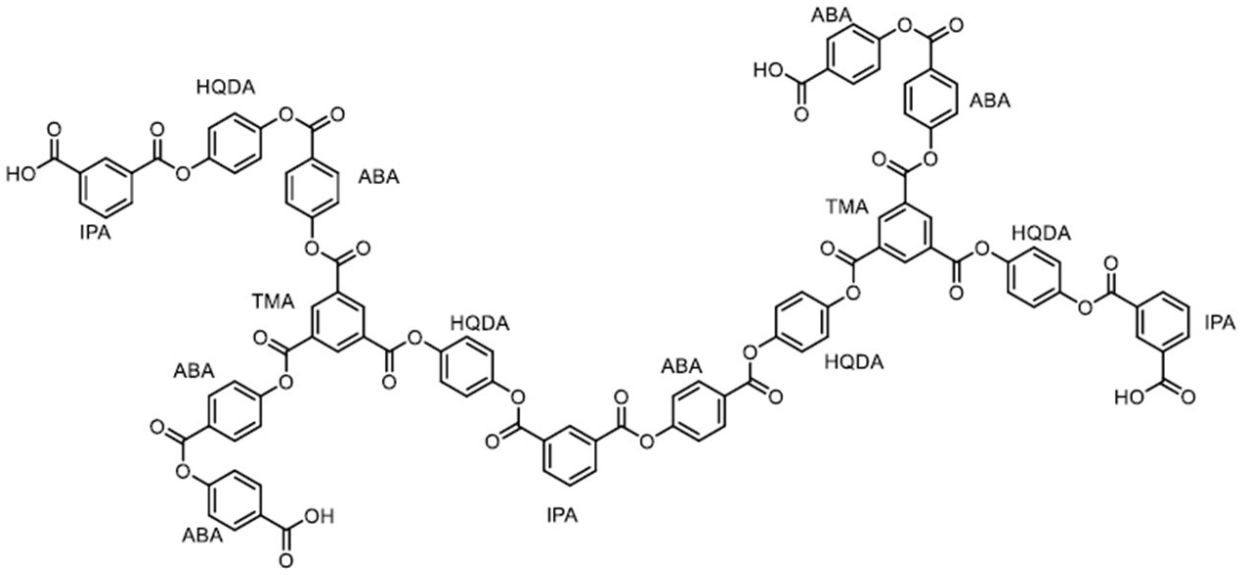

Figure S2. Chemical structure of aromatic carboxylic acid end-group oligomer

Table S1. Molar fractions of monomers used in the synthesis, and theoretical molecular weights of the acetoxy (A-group) and carboxylic acid (C-group)-capped oligomers.

Oligomer	ABA	BPDA	TMA	IPA	M_W (g/mol)
A-group	3	3	1	0	1201
C-group	3	2	1	2	1203

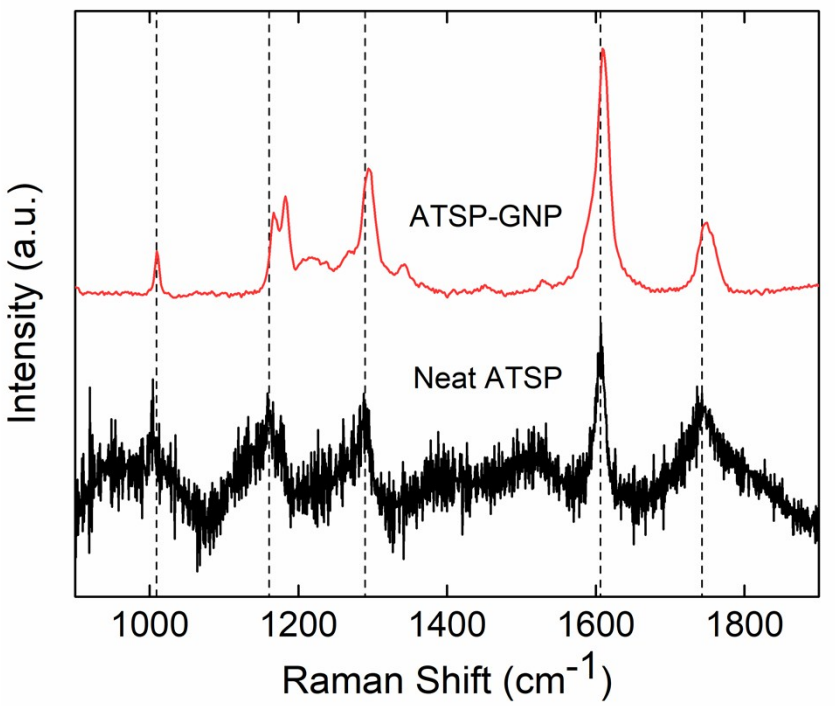

Figure S3. Raman spectra of neat ATSP and ATSP-GNP nanocomposite. Dashed lines indicate Raman peaks in the nanocomposite structure originate from the ATSP matrix.

In Figure S4, we show micro computed tomography (micro-CT) 3D reconstructed scanning images of the ATSP-GNP foam morphology nanocomposites. The micro-CT images are presented to compare the GNPs in terms of particle size for 1 μm (Figure S4.a-c), 5 μm (Figure S4.d-f), and 25 μm (Figure S4.g-i), and to evaluate them according to percolation transition characteristics for below threshold ($<\varphi_c$) (Figure S4.a, d, g), near threshold ($\sim\varphi_c$) (Figure S4.b, e, h), and above threshold ($>\varphi_c$) (Figure S4.c, f, i). For GNP 1 μm, $<\varphi_c$, $\sim\varphi_c$, $>\varphi_c$ correspond to 1 wt %, 5 wt %, and 10 wt %, respectively. For GNP 5 μm, $<\varphi_c$, $\sim\varphi_c$, $>\varphi_c$ correspond to 1 wt %, 4 wt %, and 10 wt %, respectively. For GNP 25 μm, $<\varphi_c$, $\sim\varphi_c$, $>\varphi_c$ correspond to 1 wt %, 3 wt %, and 10 wt %, respectively. For GNP 1 μm, the intrinsic porous morphology does not change with respect to the formation of the percolating network. On the other hand, GNPs of 5 μm and 25 μm demonstrate notable changes in their morphologies obtaining nearly densified structural forms. Gradual changes in the morphologies are clearly discernible in the CT images obtained for the samples near their percolation transitions (Figure S4.e and h). Both GNPs of 5 μm and 25 μm acquire densified morphologies above the percolation transitions. The modifications in the morphologies are also quantified in terms of the density, as given in Table S2. As noted, GNP 1 μm do not display any significant density change, which correlates with the CT images. Whereas, both GNP 5 μm and GNP 25 μm demonstrate significantly increased densities within their modified the nanocomposite structures. GNP 1 μm may have effective van der Waals forces between individual particles that causes them to aggregate within the matrix, so the particles may not effectively interact with the matrix yielding almost same density as neat morphology.

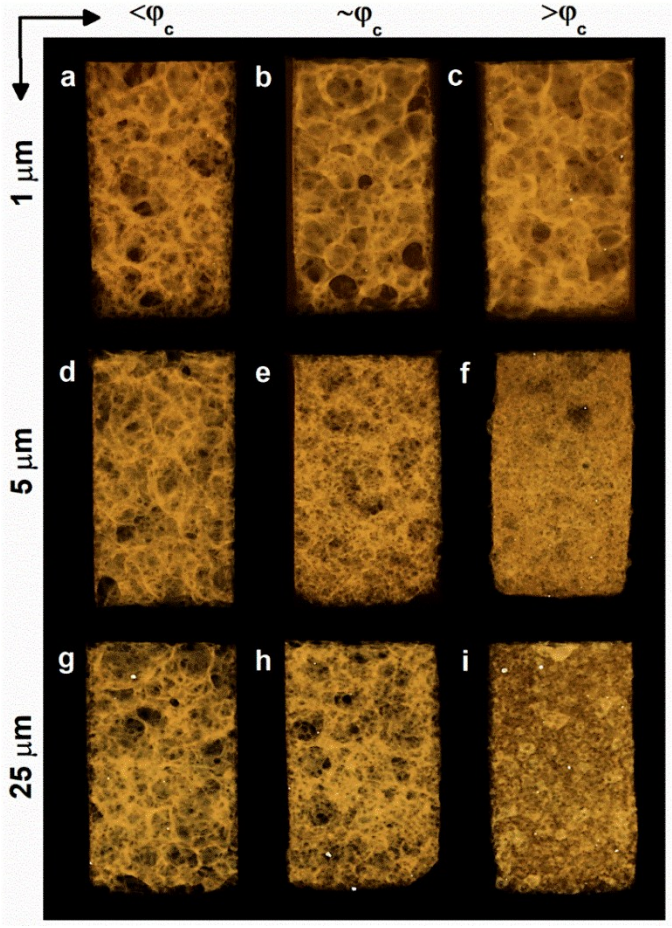

Figure S4. Micro-Computed Tomography (Micro-CT) images of the ATSP nanocomposites demonstrating variations in the porous morphology with respect to the size of 1 μm (a), 5 μm (b), and 25 μm (c) and content ($<\varphi_c$, $\sim\varphi_c$, $>\varphi_c$) of the nanofiller particles. Corresponding loading fractions are given in the above text.

Table S2. Density of ATSP-GNP foam morphology nanocomposites with respect to the size and content of the nanofiller particles. The density is given in Mg/m^3. The neat ATSP foam has a density of 0.54 Mg/m^3. The density of fully dense ATSP is 1.27 Mg/m^3. Corresponding loading fractions are given in the above text.

	1 µm	**5 µm**	**25 µm**
$<\varphi_c$	0.51±0.05	0.45±0.09	0.46±0.04
$\sim\varphi_c$	0.46±0.07	0.58±0.03	0.56±0.15
$>\varphi_c$	0.52±0.01	0.70±0.04	0.65±0.02

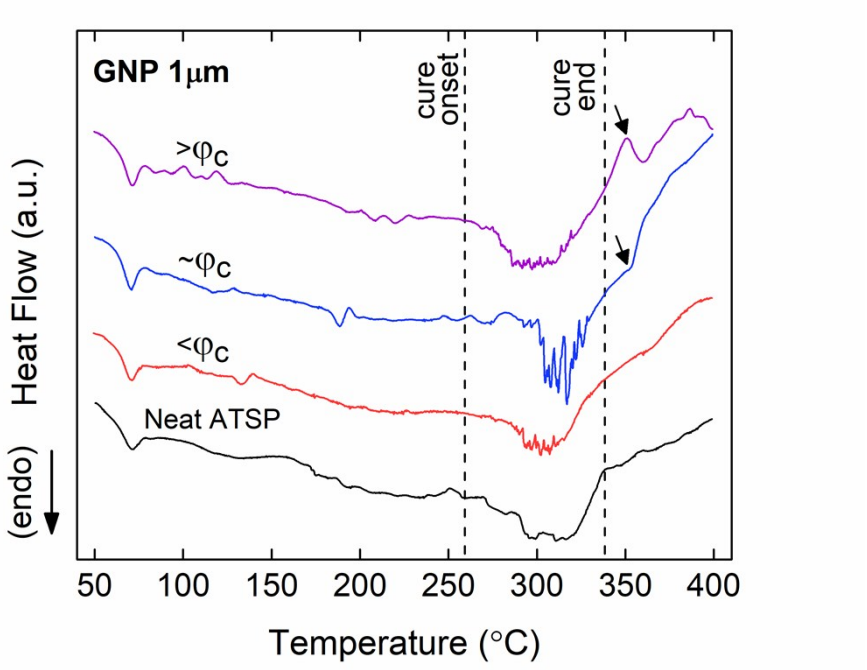

Figure S5. Differential scanning calorimetry (DSC) thermal characteristics of the condensation polymerization reaction for the combined mixtures of the precursor oligomers and GNP 1 μm at loading levels below ($<\varphi_c$), around ($\sim\varphi_c$), and above ($>\varphi_c$) electrical percolation threshold. Tests are performed under an inert atmosphere of nitrogen. The heating rate is 10 °C/min.

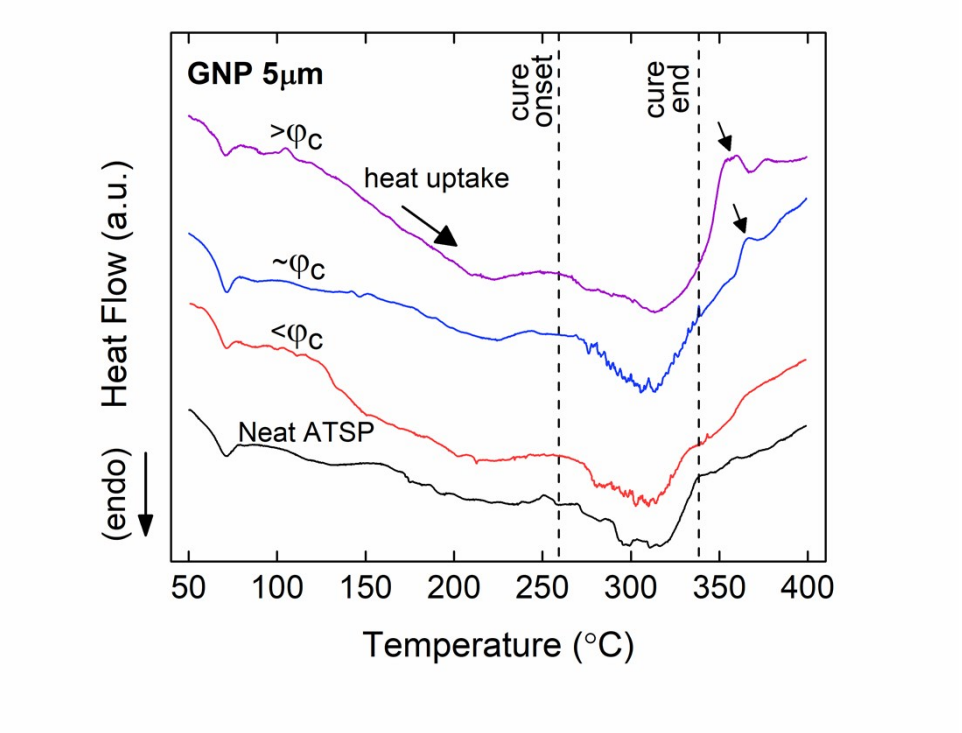

Figure S6. Differential scanning calorimetry (DSC) thermal characteristics of the condensation polymerization reaction for the combined mixtures of the precursor oligomers and GNP 5 μm at loading levels below ($<\varphi_c$), around ($\sim\varphi_c$), and above ($>\varphi_c$) electrical percolation threshold. Tests are performed under an inert atmosphere of nitrogen. The heating rate is 10 °C/min.

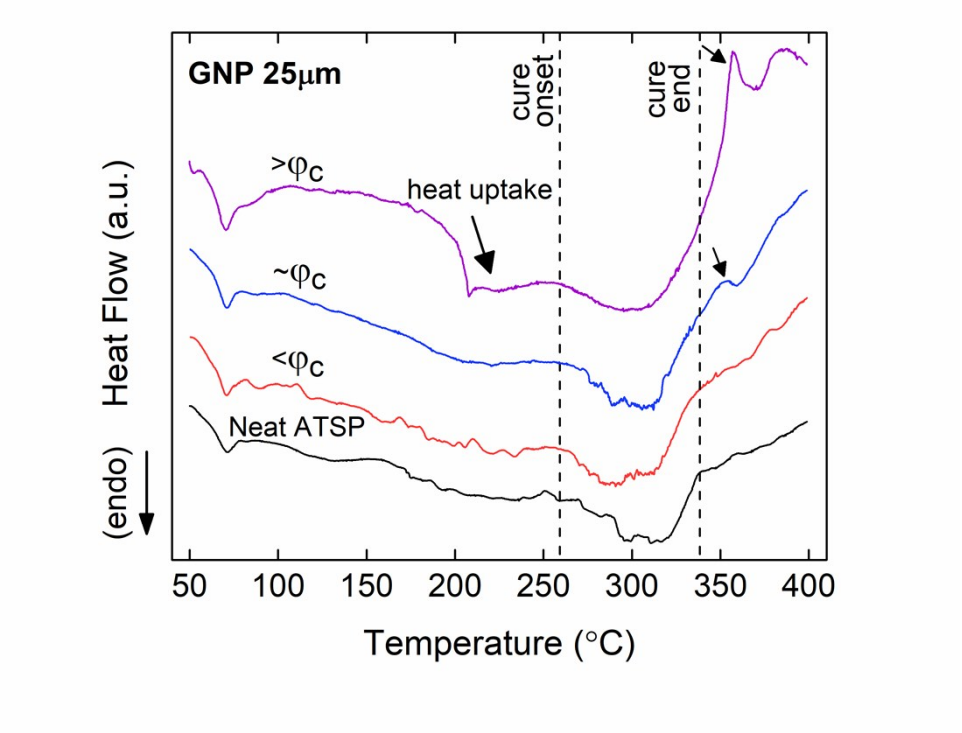

Figure S7. Differential scanning calorimetry (DSC) thermal characteristics of the condensation polymerization reaction for the combined mixtures of the precursor oligomers and GNP 25 μm at loading levels below ($<\varphi_c$), around ($\sim\varphi_c$), and above ($>\varphi_c$) electrical percolation threshold. Tests are performed under an inert atmosphere of nitrogen. The heating rate is 10 °C/min.

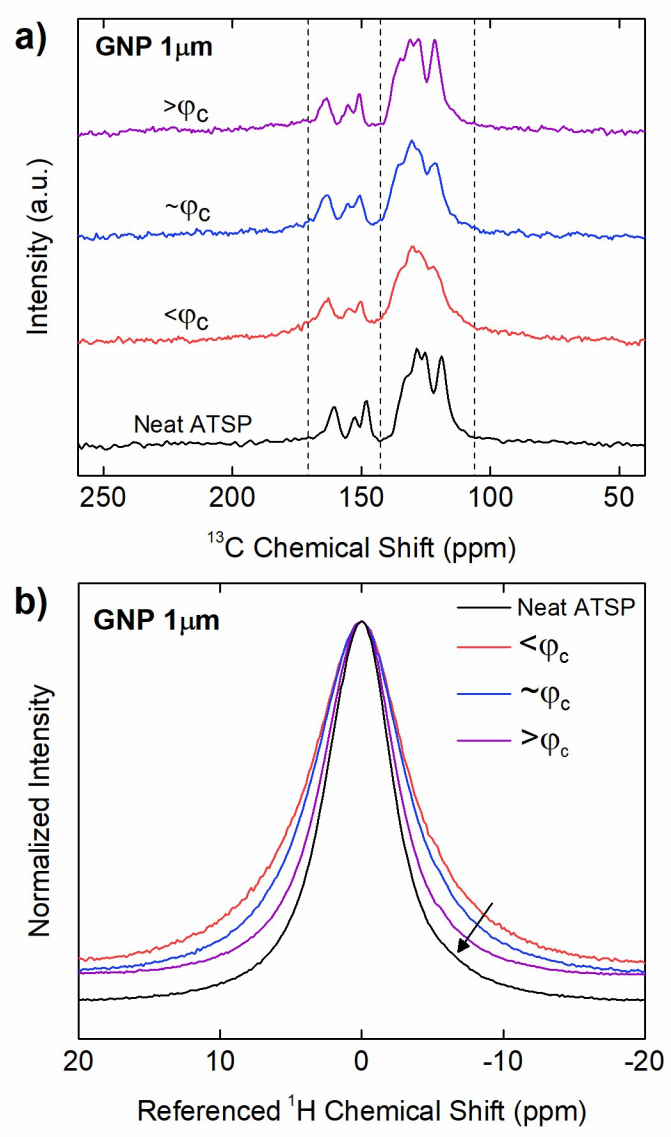

Figure S8. Solid-state Nuclear Magnetic Resonance (ssNMR) ^{13}C cross-polarization magic-angle spinning (CPMAS) (a) and ^{1}H direct pulse magic-angle spinning (DPMAS) (b) spectra of the neat ATSP morphology with respect to ATSP nanocomposites with GNP 1 μm. $<\varphi_c$, $\sim\varphi_c$, $>\varphi_c$ correspond to 1 wt %, 5 wt %, and 10 wt %, respectively. ^{13}C spectra display the GNP 1 μm nanocomposites with measured line widths of ~1347 Hz for $<\varphi_c$, ~1594 Hz for $\sim\varphi_c$, and ~1840 Hz for $>\varphi_c$ over the highest intensity peak. ^{1}H spectra exhibit the characteristic peak for $<\varphi_c$ with a line width of ~2615 Hz, $\sim\varphi_c$ with ~2727 Hz, and $>\varphi_c$ with ~1920 Hz.^{1}H and ^{13}C NMR spectra are processed using 1 Hz and 25 Hz line broadenings, respectively. The figures were given in normalized intensity axes.

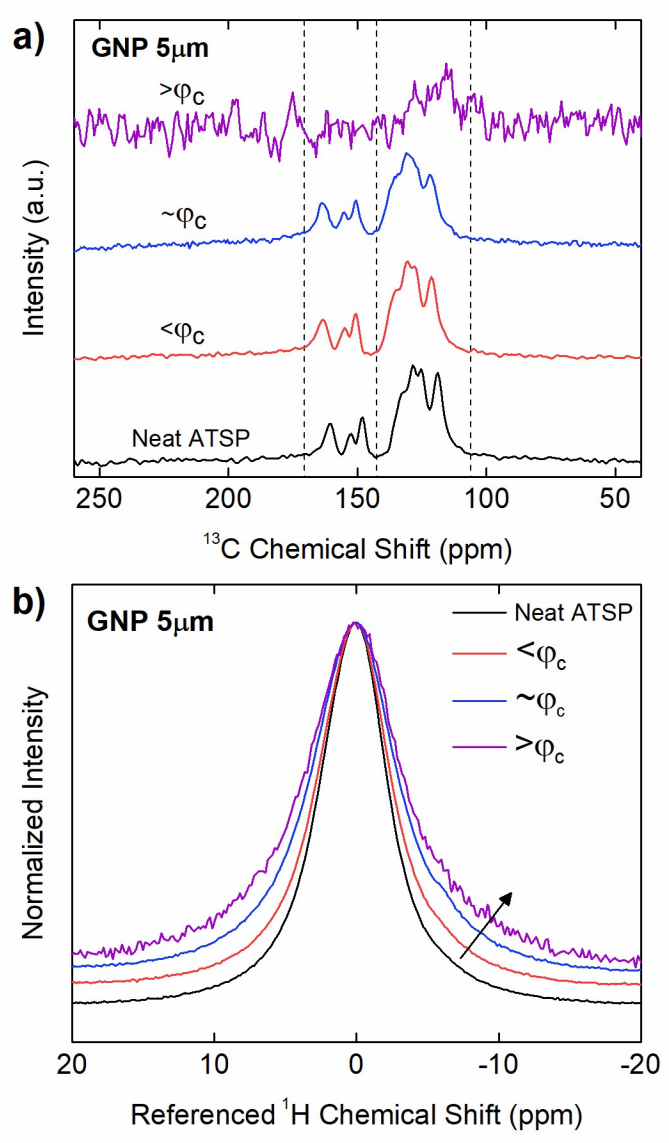

Figure S9. Solid-state Nuclear Magnetic Resonance (ssNMR) ^{13}C cross-polarization magic-angle spinning (CPMAS) (a) and ^{1}H direct pulse magic-angle spinning (DPMAS) (b) spectra of the neat ATSP morphology with respect to ATSP nanocomposites with GNP 5 μm. $<\varphi_c$, $\sim\varphi_c$, $>\varphi_c$ correspond to 1 wt %, 4 wt %, and 10 wt %, respectively. ^{13}C spectra are measured to have line widths of ~1520 Hz for $<\varphi_c$, ~1528 Hz for $\sim\varphi_c$ over the highest intensity peak, and any distinct peak formation is not observed for $>\varphi_c$ loading level. ^{1}H spectra display $<\varphi_c$ loading with ~1960 Hz line width, $\sim\varphi_c$ with ~2257 Hz, and $>\varphi_c$ with ~2353 Hz. ^{1}H and ^{13}C NMR spectra are processed using 1 Hz and 25 Hz line broadenings, respectively. The figures were given in normalized intensity axes.

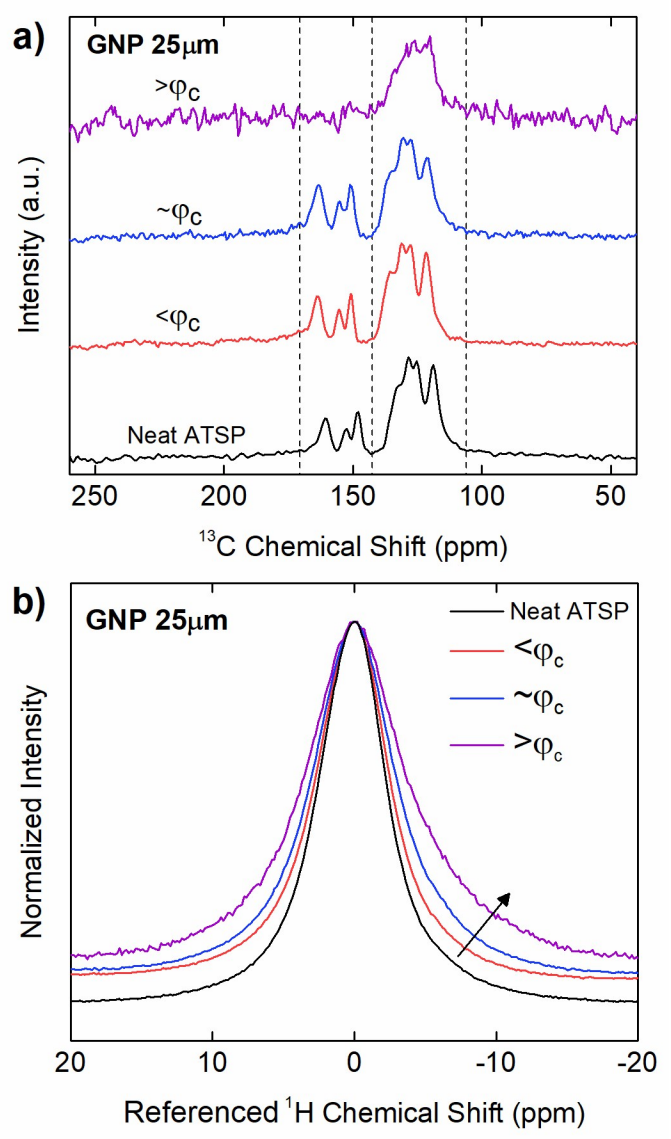

Figure S10. Solid-state Nuclear Magnetic Resonance (ssNMR) ^{13}C cross-polarization magic-angle spinning (CPMAS) (a) and ^{1}H direct pulse magic-angle spinning (DPMAS) (b) spectra of the neat ATSP morphology with respect to ATSP nanocomposites with GNP 25 μm. $<\varphi_c$, $\sim\varphi_c$, $>\varphi_c$ correspond to 1 wt %, 3 wt %, and 10 wt %, respectively. ^{13}C spectra show line widths of ~504 Hz for $<\varphi_c$, ~911 Hz for $\sim \varphi_c$, and ~1258 Hz for $>\varphi_c$ over the highest intensity peak. ^{1}H spectra demonstrate $<\varphi_c$ with a line width of ~1830 Hz, $\sim\varphi_c$ with ~2137 Hz, $>\varphi_c$ with ~2580 Hz. ^{1}H and ^{13}C NMR spectra are processed using 1 Hz and 25 Hz line broadenings, respectively. The figures were given in normalized intensity axes.